DOI 10.1007/s11106-024-00416-6
Powder Metallurgy and Metal Ceramics, Vol. 62, Nos. 9-10, January, 2024 (Ukrainian Original Vol. 62, Nos. 9-10, Sept.-Oct., 2023)

SPARK PLASMA SINTERING OF Al_2O_3 REINFORCED ALUMINUM ALLOY METAL MATRIX COMPOSITES (REVIEW)

Ananth S. Iyengar[1] and R. Suresh[1,2]

UDC 536.421.5:621.365.32:546.(62+62'21):539.4.015

Aluminum matrix nanocomposites (AMNCs) are a distinct category of advanced materials that incorporate nanoscale reinforcement in a ductile material matrix. Various nanomaterial reinforcements for AMNCs have been reported in the literature, including multi-walled carbon nanotubes (MWCNT), graphene nanoplatelets, silicon carbide, and boron nitride. These classes of materials have been described to exhibit both improvements and reductions in mechanical properties. The interfacial material phases result in low-strength materials. Improvements in mechanical properties are attributed by refined grain size and shape for both the matrix material and the reinforcement agent. These materials demonstrate higher hardness, yield strength, and wear corrosion compared to conventionally prepared aluminum composites. Spark plasma sintering (SPS) is one of the non-conventional sintering methods used to prepare metal matrix composites, resulting in fully dense composite materials. The SPS-produced metal matrix composite can be manufactured rapidly and finds its applications in the automotive, aerospace, and defense industries. This review provides an overview and current status of metal matrix composites regarding matrix and reinforcing materials and the SPS process for producing metal matrix composites.

Keywords: *spark plasma sintering, aluminum metal matrix composites, aluminum oxide, hardness, ultimate strength, yield strength.*

INTRODUCTION

Advanced materials, including metal matrix nanocomposites (MMNCs), have proven invaluable in key industrial applications due to their superior mechanical properties. MMNCs are attractive because the material can be tailored to produce materials with tunable thermal, mechanical, optical and physical properties. Typically, MMNCs are a combination of matrix metal mixed with a small percentage of nanomaterial reinforcement. Aluminum and alumina MMNCs have been studied for a variety of mechanical and optical properties [1–4].

Aluminum has a low melting point, easy formability, light weight, high thermal and electrical conductivity, and corrosion resistance, which make it an ideal candidate for metal matrix nanocomposites. Aluminum MMNCs reinforced with carbon nanotubes (CNTs) and ceramic nanoparticles have shown a great potential as they exhibit improved hardness and wear resistance. Alumina MMNCs can be used in higher temperature applications compared

[1]Department of Mechanical and Manufacturing Engineering, M.S. Ramaiah University of Applied Sciences, Bengalore-560058, India.

[2]To whom correspondence should be addressed; e-mail: sureshchiru09@gmail.com.

Published in Poroshkova Metallurgiya, Vol. 62, Nos. 9–10 (553), pp. 42–64, 2023. Original article submitted September 7, 2023.

to aluminum MMNCs. The MMNCs can be prepared by stir casting and powder sintering techniques [5]. The advantages and disadvantages of each of these techniques have been reviewed in the literature [6].

The preparation of MMNC by the stir-casting method is less expensive, has the flexibility of component shapes, and is suitable for large-scale production industries. The stir casting method for MMNC preparation depends on the casting parameters, including the temperature of the melt, the density difference between the reinforcement and the matrix metal, the high-temperature reactions, and the stirring speed. The effects of these process parameters on the final product are difficult to control [6]. The MMNC prepared by the stir casting technique suffers from non-uniform distribution of reinforcement due to buoyancy forces, agglomeration, wettability, and high-temperature reactions. MMNCs prepared by powder metallurgical techniques have unique advantages, including the product being completely dense, with mechanical property improvements.

The powder metallurgy process can easily blend reinforced nanomaterials that are incompatible with the matrix in the stir casting process. MMNCs produced by powder MMNC are conventionally hot pressed to produce a green sample, which is then sintered. This process is plagued by grain growth during sintering and weak interparticle bonding.

Spark plasma sintering (SPS) has been reported to increase the hardness of 6061 and 2124 aluminum alloys compared to other forms of sintering. SPS also consistently produces higher-densified samples than microwave sintering [7].

MATERIALS AND SPS PROCESS

The SPS process is well documented in the literature [8, 9]. As shown in Fig. 1, SPS involves the use of an electrically conductive die such as a graphite die and punch. Other die materials reported include Co/WC composite [10]. A graphite sheet or a solid lubricant such as zinc stearate is applied to the inner surface of the die wall [11]. The powder mixture of matrix and reinforcement to be sintered is placed in the die press assembly. The entire assembly is placed in a vacuum or inert gas environment at pressures of a few Pascals. A low voltage, high amperage pulsed current is activated to flow through the sample while simultaneously compressing it at moderate pressures.

Heat generated by the SPS technique is both *in situ* and external. The *in situ* heat source is the joule heating in the sample, while additional heat is generated by the joule heating of the die and press, and heat generation also occurs in the powder sample due to its electrical resistance. The sintered samples are affected by the sintering process parameters such as vacuum environment, sintering temperature, applied pressure, dwell time and temperature ramp. Near net shape samples produced by the SPS technique are described in the literature [12].

Table 1 briefly reviews the literature on SPS processing of aluminum, aluminum alloy, and alumina particles, including aluminum scrap powder. Ball milling of powders is the most preferred method for homogeneous mixing of these particles. However, ball milling for long periods of time results in a reduction in the length of the CNTs, which may limit the improvement in the properties of composite samples [13]. The pulverized particles are dispersed in organic solvents such as ethanol, isopropyl alcohol, dimethylformamide (DMF), acetone, and stearic acid. Ultrasonication is used to uniformly disperse the matrix and reinforcement particles.

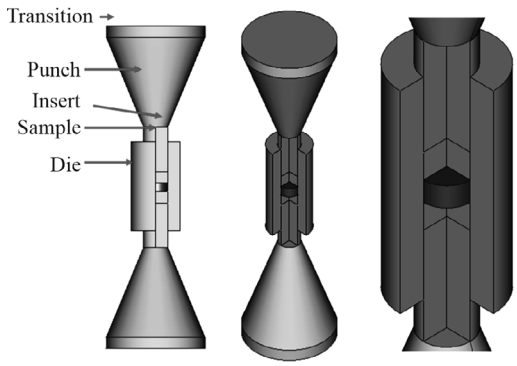

Fig. 1. Schematic cutaway view of the setup of the SPS die assembly

TABLE 1. Overview of Different Al-Matrixed Reinforcements and Process Parameters Used in the SPS Process

References	Matrix and reinforcement	Dispersion method	SPS parameters	Density, %	Measured properties
[11]	Matrix: Al; reiforcements: 20 and 30% Si, and 40% Si + 0.5 CNT	Ball milling	Sintering temperature 500–550 °C; ramp 100 °C/min; time 10 min; pressure 30–40 MPa	82.2	Compression strength 129 MPa at 500 °C for 30% Si, 250.24 MPa at 550 °C for 30% Si
[22]	Matrix: aluminium; reinforcement: 1% SiC	Mechanical (ball milling 24 h)	Sintering temperature 600 °C; ramp 200 °C/min; time 10 min; pressure 50 MPa	95	Compressive strength 312 MPa; microhardness 108 MPa
[27]	Matrix: aluminium; reinforcement: CNT	Acetone + ultrasonication	Sintering temperature 500 °C; ramp 50–60 °C/min; time 60 min; pressure 80 MPa	99.9	Ultimate tensile strength is reported to 40% increase and elastic modulus exhibits an increase of 65% over the pure Al for 1 vol.% CNT sample
[35]	Matrix: Al_2O_3 nanoparticles; reinforcement: 0.1% CNT	Ethanol + ultrasonication	Sintering temperature 1,500 °C; time 3 min; pressure 80 MPa	97.9–99.97	No appreciable increase in the: fracture toughness ($MPa \cdot m^{1/2}$), hardness HV0.5 (GPa)
[36]	Matrix: Al_2O_3, ZrO_2, Y_2O_3 reinforcement: SWCNT, MWCNT 0.1 to 1%	Ethanol ultrasonication + mortar mixing	Sintering temperature 1520 °C; ramp 80 °C/min; time 5 min; pressure: 80 Mpa	>98	Vickers hardness 18–22 GPa; fracture toughness 4–8 ($MPa \cdot m^{1/2}$)
[37]	Matrix: Al_2O_3; reinforcement: MgO doped		Sintering temperature 1,050–1,100 °C; ramp 100 °C/min; time 10 min; pressure 400 MPa		Clear optical properties
[38]	Matrix: Al_2O_3; reinforcement: ZrO_2 + Mullite	Plasma sprayed + ball milling	Sintering temperature 1000–1300 °C; time 10 min	>99.5	Hardness: 960 to 1,266 $kgf \cdot mm^{-2}$; Young's modulus: 146–208 GPa; fracture toughness 2.51–11.21 $MPa \cdot m^{1/2}$
[39]	Matrix: $AlMg_5$; reinforcement: 0.4% Al_2O_3		Sintering temperature 550 °C; ramp 100 °C/min; time 15 min; pressure 50 MPa	98	Unmilled compression strength 132 MPa; milled SPS compression strength 242 MPa (unmilled is lower because of large particle size)

Continued TABLE 1

References	Matrix and reinforcement	Dispersion method	SPS parameters	Density, %	Measured properties
[40]	Matrix: Al 5083 alloy powder; reinforcement: 10% SiC nanoparticles	Ball milling with stearic acid at 400 rpm	Sintering temperature 500 °C; ramp 100 °C/min; time 3 min; pressure 50 MPa	Near theoretical densities	Compression test reveals, hardening due to ball milling, and addition of SiC particles. MMC properties includes hardness of ~280 HV with an elastic modulus of 126 GPa
[41]	Matrix Al; reinforcement: GNP (0.5, 1, 3, and 5%)	Acetone + ultrasonication	Sintering temperature 550 °C; time 40 min; pressure 50 MPa	98.3–99.8	Yield strength improvement of 84.5% and ultimate tensile strength improvement of and 54.8%, is reported for 1% composition
[42]	Matrix: aluminium; reinforcement : Al_2O_3 (0.5, 1, 3, 5, 7%)	Mortar mixture	Sintering temperature 500 °C; ramp 80 °C/min; time 5 min; pressure 80 MPa	90.1–99.5	Nanoindentation process yields 0.85 GPa as the hardness value for 7% inclusion
[43]	Matrix: AA2124	Ball milling	Sintering temperature 480 °C; ramp 100 °C/min; time 10 min; pressure 60 MPa	>95.5	Vickers hardness nanopowder 155.5; micropowder 250.2; compressive strength nanopowder 703 MPa; micropowder 300 MPa
[44]	Matrix: aluminium; reinforcement: boron nitride 0.5, 1.5, 3, 4.5, 6, and 7.5 wt.%	Isopropyl alcohol + sonication	Sintering temperature: 600 °C; ramp 60 °C/min; time 5 min; pressure 60 MPa	>97	Tensile yield strength 115 MPa; 50–75% increase in properties
[45]	Matrix: aluminium 1056; reinforcement: 15% zircon	Ethanol in turbula mixer	Sintering temperature 450 °C; time 4 min; pressure 40 MPa	99.3	Bending strength 284 MPa; microhardness 171 VHN
[46]	Matrix: aluminium 1056; reinforcement: 10% vanadium carbide	Ethanol in turbula mixer	Sintering temperature 450 °C; time: 10 min; pressure 30 MPa	99	Bending strength 295 MPa; microhardness 232 MPa
[47]	Matrix: Al_2O_3		Sintering temperature 1,000 °C; ramp 70 °C/min; time 10 min; pressure 500 MPa	>99	Clear optical properties; anisotropic optical properties
[48]	Matrix: Al; reinforcement: 2–5% CNT; 2% carbon black	Ball milling, in dimethylformadie	Sintering temperature 500–550 °C; ramp 100 °C/min; time 10 min; pressure 30–40 MPa	>67	Electrical conductivity 300–600 S/m

Variations in the densification behavior of aluminum composites are observed with SiC reinforcement at 30 to 40% composition [11]. The relative densities (RD) for these composites decrease with increasing SiC concentration, from RD 95% for 20% SiC to RD 88% for 50% SiC inclusion. The reinforcement material such as high aspect ratio carbon nanotubes is more prone to agglomeration due to entanglement [14]. In particular, the agglomeration of the reinforcing CNTs is a limitation for improving mechanical and thermal-physical properties of sintered composite samples. Jagannatham et al. report that the copper-coated CNTs have a better homogeneous dispersion compared to the uncoated CNTs, resulting in lower mechanical properties [13]. These reinforcements need to be disentangled, and popular methods for disentanglement include the use of surfactants such as sodium dodecyl sulfate, surface charge modification, and wet coating methods [6]. The surface of reinforcing particles can be modified using acid oxidation methods [15]. Esmaeilzaei et al. have reported SPS consolidation of cobalt coated Al_2O_3 and TiO_2 ceramics. They report that the sintering process is performed by melting and liquid phase of metallic cobalt, which minimizes the direct contact of the ceramic particles with the cobalt layer [16].

Other methods of incorporating reinforcements include physical mixing, spray drying [17, 18], chemical methods such as wet chemistry, polymer melt blending [19], rubber blending [20], and microscale methods such as plasma spraying [21]. In plasma spraying, plasma is generated by applying a high voltage differential, ionizing the arc gas, and causing the matrix and reinforcing spray particles to form. The splatting of the CNT and matrix spray particles produces the mixing of reinforcement and matrix. In the polymer-assisted method, the CNTs are mixed with a molten polymer to form a slurry. Aluminum powder is then mixed with the slurry in a screw extruder to provide mechanical shear mixing. The extruded mixture of polymer, reinforcement, and aluminum matrix particles is then heated. This causes the polymer to decompose and evaporate [19]. Other common reinforcements include SiC, TiC, Al_4C_3, WC, TaC, TiB_2, AlB_2, AlN, and Al_2O_3 have been used with aluminum as listed in Table 1. These reinforcements exhibit better wettability with aluminum and are much easier to mix with the matrix than CNTs. Due to the mixing of the nanoparticle reinforcement with the micro-particle matrix material, the reinforcement is only in the particle boundary regions [22].

Several researchers have reported the SPS process on prepared particles such as tungsten coated diamond particles [23], copper coated CNT in aluminum [13], high entropy alloy CoCrFeMnNi nanoparticles in aluminum alloy [24], niobium [25], and $Nd_2Ti_2O_7$ [26]. The final sintered sample is also affected by the percentage of filler material. It is reported that as the percentage of inclusion is increased, the thermal conductivity of the aluminum–diamond composite shows an increasing trend. At higher concentrations, the thermal conductivity has a maximum and the trend decreases. This could be attributed to the increased number of grain boundaries due to higher particle inclusion percentage [23]. The surface layer of the reinforcing particles is reported to play an important role. Researchers have coated tungsten on diamond [23] to improve the thermal properties of the composite. Increased micro-hardness in aluminum–CNT composites with copper coating on CNTs is reported by Jagannatham et al. The uncoated CNT composite sample shows lower micro-hardness at 2% reinforcement, while the coated sample shows much higher hardness by inhibiting Al_4C_3 formation. One factor that improves the mechanical properties of the sample is the aspect ratio of the reinforcement. Carbon nanotubes (CNTs) with a higher aspect ratio at lower concentrations lead to improved strengthening of Al–CNT composites, according to Boesl et al. The longer CNTs produce local stiffening and the lower concentration produces less opportunity for Al_4C_3 content [27].

The SPS process parameters as a function of time for aluminum particles are given by [28] and are illustrated in Fig. 2. It can be seen that the initial phase (up to 10 min) of the SPS process involves rapid heating of the sample powder and the die assembly. The voltage and current are continuously increased with a steady increase in temperature. Pressure and displacement are moderately increased during this phase. Necking and sparking at the particle boundaries occur at the end of the initial phase. In the subsequent phase, the displacement increases at a much higher rate. This is due to the fact that aluminum has a much lower internal stress for the induced strain above 400°C [29]. As the temperature reaches the target point of 500 to 550°C, the consolidation of the particles also peaks. The sample density reaches more than 95% of the bulk aluminum. The strain behavior of micro-particles is very different from that of nanoparticles, as reported in the literature for most materials [30, 31]. Since the nanoparticles have a higher surface area to volume ratio, the surface effects and the oxide layer on the particle

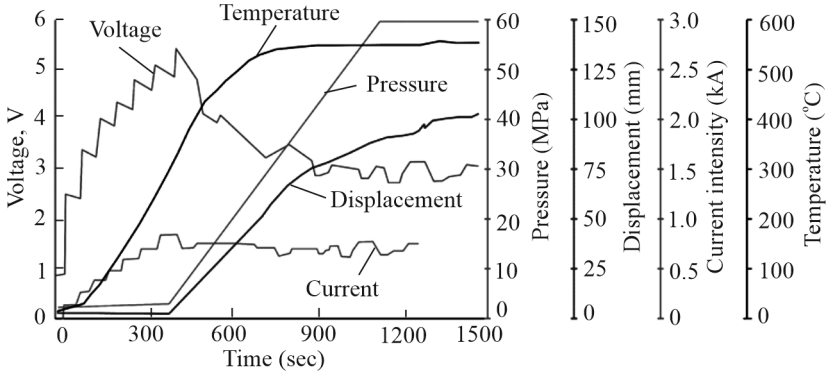

Fig. 2. Combined process parameter graph for aluminum SPS process

surface play an important role in the strengthening. In addition, it has been reported that the concentrations of oxygen and hydrogen in the samples decrease with the increase of the processing temperature of the SPS [32]. The effect of surface oxygen is reduced for 180 μm diameter particles, while smaller diameter particles experience greater surface oxygen influence. Furthermore, increasing SPS processing temperature may not decrease oxygen and hydrogen concentrations significantly with temperature [32, 33].

Similar to the compaction behavior of aluminum, Al_2O_3 shows a consolidation in SPS method at temperatures above 1,600°C. The consolidation of alumina micro- and nanoparticles with SiC filler material has been reported by [34]. They record final densities of approximately 99% for microparticles and 92–94% for nanoparticles. A pulsed current intensity of 1 to 3.5 kA is used with a pressure of 20 MPa and a soaking time of 10 min. The SPS technique has been used by several researchers to prepare translucent, crystal-like materials from alumina particles [35–38].

A correlation analysis shows that all these parameters are positively correlated between displacement, pressure, temperature, current, and voltage. The pressure–voltage and pressure–displacement pairs are the parameters that show perfect positive correlation.

This analysis also shows a high correlation between temperature and current, but not between temperature and voltage, as would be expected. The dielectric breakdown and arcing between the particles is a function of the applied voltage. Joule effect of the current flowing through the die assembly is responsible for the heating.

FACTORS AFFECTING THE SPS TECHNIQUE

SPS is a complex solidification process that involves several physical phenomena such as Joule heating, particle solidification due to uniaxial pressure, heat transfer, particle sparking, and electrical and magnetic flow through the specimens. In order to understand the material behavior and the process parameters, some researchers have performed finite element analysis (FEA) on the SPS technique. Giuntini et al. conducted a study on SPS tool design using the COMSOL Multiphysics approach with resistive contacts between the abutting surfaces [49, 50]. They report that a 2-spacer tool is better than a 4-spacer configuration [12].

Vacuum Environment and Die System. Oxidation of materials during sintering must be avoided to improve particle bonding and mechanical properties of the samples. Microparticles have lower oxidation effects compared to ZrB_2+SiC nanoparticles in SPS technique due to the high surface-to-volume ratio in nanoparticles. It is reported that purging the environment with argon can reduce the effects of oxide formation in ZrB_2+SiC nanoparticles in the SPS technique [51]. In particular, aluminum has an oxide layer about 4 nm thick. This oxide layer is embedded in the interstitial spaces between the particles during the consolidation stage of the SPS process. The embedded surface aluminum oxide increases the hardness of the SPS sample up to 10% [52]. A similar trend is reported for the argon-purged SPS technique applied to graphene nano-platelet-reinforced aluminum nanocomposite [41]. The SPS process carried out in a vacuum condition involves using a vacuum of $5–10^{-2}$ to 10^{-4} mbar [8]. The vacuum environment effectively stops the oxidation of the particles at elevated temperatures but does not remove the oxide layer already present on the particle surface.

Sintering Temperature and Temperature Ramp. The role of dwell temperature in the densification of aluminum microparticles by SPS has been studied at a wider temperature range of 280 to 540°C [53]. Further [53] reported that complete densification occurred at about 500°C. Khalil et al. have carried out SPS densification of Al6061 and Al2124 pre-alloyed powders with an average particle size of about 10 μm. The SPS process was carried out at temperatures of 400, 450 and 500°C. It is reported that temperature is the most influential parameter in SPS of these alloys. A completely dense SPS aluminum sample is obtained at a temperature of 450°C and a pressure of 35 MPa.

It is also stated that an increase in pressure has a detrimental effect on grain growth, leading to a decrease in hardness [54]. It can be observed that the alloying elements in the pre-alloyed powders have a significant influence on the densification behavior of SPS. A decrease in the consolidation of aluminum as a function of temperature has been reported for different concentrations of composite particle inclusion [55]. In particular, AlN modified the consolidation behavior the least, but SiC, Si_3N_4, and BN show more alterations. The lowest density was observed in the presence of 10% boron nitride inclusions in the alumina MMC. Creep behavior for alumina in the temperature range of 1,125 to 1,250°C in the stress range of 80 to 120 MPa is reported in the literature [56, 57]. Consolidation behavior based on pressure and creep behavior of materials has been reported in the literature [58]. Further refinement of the developed model to account for the consolidation behavior of SPS due to alloying and inclusion of composite particles will be required for development and validation.

The effect of a heating ramp on copper, aluminum, Al_2O_3 composites has also been described in the literature [3]. Temperature ramping cause's instantaneous densification [9, 15, 59–61]. The necking behavior in copper and alumina particles is reported by [62]. The classical kinetic laws and Coble creep models are reported to be effective in understanding thermal diffusion and plastic-yielding behavior of corundum micro particles due to temperature ramp [3]. Local heating in the particle interface at high heating rates was reported to be nearly 3 to 10 times as high as at lower heating rates [3]. The heating rate should be selected based on the grain size. Smaller grain size achieves better densities at lower heating rates.

SPS Pressure. Breaking through the oxide layer present on metals such as aluminum is the primary advantage of using pressure in the SPS process. Using graphite material for the die and punch, SPS process pressures can be as high as 50 MPa [33]. Mizuuchi et al. have achieved 300 MPa using electrically conductive tungsten carbide/cobalt dies [10]. As the applied pressure or load increases, the grain size in the sintered specimens is reported to increase [57]. The grain growth is mainly due to the phenomenon of grain boundary diffusion when the temperature is high enough. An average grain size of Al_2O_3 sample sintered at 10 MPa is reported to be 4.3 μm, and a grain size of 7.3 μm is reported at a higher pressure of 100 MPa [57]. The combination of pressure and electrostatic sparking leads to partial rupture of the oxide layer and improves the electrical conductivity of Al MMCs [53]. The improvement in thermal and electrical conductivity of the particle aggregates in the early stages of the SPS process is due to the formation of diffusion and reaction bonds between the particles. The conventional hot pressing method relies on the high temperature and grain boundary diffusion, it is important to note that SPS technique uses plasma sparks due to high current electric discharge.

Moreover, the pulsation of the direct current causes the consolidation of the melt in diamond–aluminum system [63], and titanium–aluminum [64]. The presence of Al_2O_3 and Al_4C_3 compounds at the interface has been reported [63]. In particular, the reaction between Al_2O_3 and carbon at sintering temperatures of 620°C has been proposed as the mechanism for the formation of Al_4C_3 [6]. The interfacial Al_4C_3 structure at the interface is more brittle than the aluminum matrix and is typically 100 nm to a few microns in size, depending on the reaction conditions [63]. In the case of carbon nanotube (CNT)-aluminum composites, this aluminum carbide formation reaction can completely consume the CNT, leading to conflicting results reported in the literature [43]. In the case of optically clear sintered specimens using Al_2O_3, the pressure is expected to be higher because the grain sizes must be larger with a slow recrystallization rate so that the microcrystalline dimensions are smaller than the wavelength of visible light. This is achieved in the SPS of Al_2O_3 by using high pressures of 500 MPa and a slow cooling time [37, 47, 57].

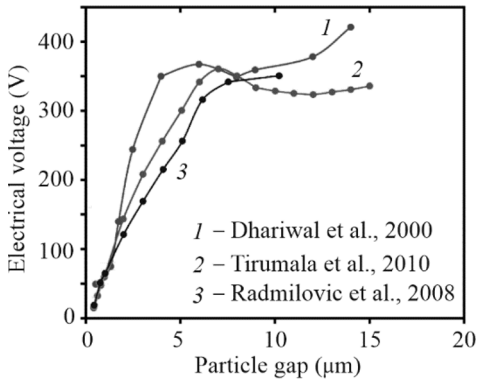

Fig. 3. Electrical breakdown voltage vs. interparticle distance

Influence of Electrical Pulse Pattern. Khor et al. [38], discuss the possibility of high-temperature sputtering phenomenon and surface cleaning generated spark impact pressure during the SPS process. However, partial fracture of surface oxides has been shown in the consolidation results of aluminum scrap particles [52]. Furthermore, the SPS samples exhibit higher hardness values than the aluminum due to the presence of an oxide layer [52]. For a given temperature and pressure of the experiment, the pulse width and frequency are reported to have a negligible effect on the grain size and density of the samples [57]. However, Olevsky et al. argue that higher frequencies result in larger temperature gradients due to insufficient time for heat transfer and thus promote thermal diffusion. In the early stages of SPS, the high-frequency pulse produces better thermal diffusion and promotes necking. However, in the final stages, the pore size may produce larger vacancies that hinder the sintering process [65].

Microscopic View of the SPS Process. Particle behavior at the microscopic length scale can have a significant effect on the electrical, optical, and mechanical behavior of the consolidated bulk sample. Based on several parameters such as gap spacing, voltage, surface oxide layer, and surface geometry, the interparticle region exhibits sparking, necking, and electrical contact formation [62]. Paschen's law is the analytical formulation for breakdown voltage was first proposed by Paschen, several modifications of this theory are proposed in the literature [66–68].

As shown in Fig. 3, the breakdown voltage is lower for smaller gaps. It reaches about 350 V for a gap of 8 to 10 μm. All conductive materials form an unconventional "necking" at this condition. This is characteristic of mass transfer along the electrical spark.

Taken together with the correlation results of Figs. 2 and 3, we understand that in the SPS process of aluminum particulates, the high current flow warms the sample powder to near the glass transition temperature in a few minutes, and the electrical resistance in the particulate aggregate, due to the interparticle distance of a few 100 nm, exhibits an arc due to the applied voltage, leading to the Townsend mechanism. However, by applying pressure and elevated temperature during this stage of the SPS process, deformation of the particles occurs and the gaps and voids between the particles are reduced.

Another exponential consolidation phase occurs as the sample temperature approaches the glass transition temperature. However, the formation of unbonded, diffusion bonded, and reaction bonded contacts occurs due to the presence of an oxide layer at the particle and grain boundaries. Olevsky et al. report a mathematical model to describe the thermal diffusion behavior during SPS technique [65]. Thermal diffusion is more pronounced for smaller alumina particle sizes. Model prediction also indicates that thermal diffusion is comparable to external pressure creep binding at higher temperatures [69, 70].

Ageing of the SPS-ed Compact Samples. The microhardness evolution during ageing of SPS-treated Al7075 gas atomized particles has been reported by Molnorova et al. They annealed SPS samples at temperatures ranging from 150 to 500°C. Overall, coarse grains and a large number of low angle boundaries are produced by annealing the SPS sample. They report a reduction in microhardness for samples annealed at intermediate temperatures of

250, 300 and 350°C due to precipitation of $\eta - Mg(Zn, Al, Cu)_2$ alloy and subsequent growth. However, at annealing temperatures higher than 350°C, the alloy is partially dissolved, as evidenced by the recovery of the micro-hardness of the sample. Long-term ageing (500 days) shows a significant improvement in the micro-hardness of the samples annealed at 500°C. The samples annealed at lower temperature do not show a moderate increase in micro-hardness for long term annealing [71].

MATHEMATICAL MODELING OF SPS TECHNIQUE ON ALUMINUM AND ALUMINA POWDERS

Several researchers have proposed closed-form mathematical models for the understanding of the SPS technique as applied to conductive metal powders. The prediction of density, grain size, has been reported based on the theory developed for the hot isostatic pressing process [57]. In brief, the instantaneous effective stress on the particle bed and the shear modulus of elasticity are calculated by means of empirical correlations. Stress values are recalculated for the stages of the SPS process, including initial heating, exponential temperature rise, and densification at high temperature [57]. Olevsky et al. developed a microscopic model to predict power-law creep, grain boundary diffusion driven by external load and surface tension, and thermal diffusion enhancing densification during SPS [65]. Thermal diffusion can be significant for small particle sizes and can explain shrinkage kinetics in alumina powder sintering according to the model of Olevsky et al. (2009). Discrepancies are attributed to neglected electromagnetic effects in modeling [65].

Yield strength prediction by shear lag, Orowan looping mechanism, and rule of mixtures have been proposed in the literature [72–74]. Shear lag model is reported to over predict the yield strength of GNP-reinforced aluminum composite, while Orowan looping mechanism is reported to slightly under predict the yield strength, and rule of mixtures also slightly over predicts the yield strength [75].

The densification behavior was estimated using regression approach [58], and FEA approach was applied to simulate the SPS process within an electro-thermal module of COMSOL Multiphysics software. A brief review of the FEA approach applied to the SPS technique is given in Table 2. The FEA method is capable of elucidating the internal temperature variations in cylindrical and complex shapes, densification mechanisms, die material effect, predicting hardness, and microstructure evolution during the SPS process.

Achenani et al. have investigated the internal temperature variation during the SPS process, they report that an aluminum sample can have temperature variations close to 20°C for 30 to 40 mm diameter sample [76]. The electrical behavior of the die, punch, and powder sample was investigated, and it was concluded that since no phase shift was detected during the pulsing of the current, purely resistive heating occurred [49].

TABLE 2. FEA analysis of SPS technique

Sl. No.	References	Software used	Remarks
1	Achenani et al. [76]	COMSOL	Internal radial temperature gradient, graphite felt is used to reduce the gradient
2	Pavia et al. [49]	COMSOL	Die material properties influence on the sample
3	Maniere et al. [79]	COMSOL	Densification behavior for complex shape with sacrificial die design
4	Maniere et al. [80]	COMSOL	Densification behavior for complex shape
5	Munoz et al. [77]	–	Evolution of temperature gradients, densification
6	Giuntini et al. [12]	–	Densification, localized overheating
7	Molenat et al. [50]	–	Temperature control
8	Guillon et al. [61]	–	Tooling, temperature
9	Xiong et al. [81]	–	Microstructure evolution
10	Bolzon et al. [78]	–	Hardness simulation
11	Olevsky et al. [82]	–	Temperature distribution in a complex geometry and correlations with electrical behavior

Pavia et al. also report that the graphite properties change during the experiment depending on the temperature and pressure applied [49]. Munoz et al. reported that the magnitude of the stresses in the powder samples depends on the difference in thermal expansion of the sample and the die material when simulating the SPS process for alumina and copper samples. The inhomogeneous stress distribution in both axial and radial directions is reported to be due to the displacement and simultaneous heating of the powder samples [77]. The densification behavior of powders is reported to be directly affected by the stress distribution.

Bolzon et al. have simulated the Rockwell hardness test for Al/TiB_2 and Al/ZrO_2 composites to verify the suitability of applying the classical Hencky–Huber–Mises model and Drucker–Prager models are suitable for metal matrix composites. Even in the elastic mode, these models were found to be incapable of explaining the deviations caused by the microstructure of metal matrix materials [78].

CREATION OF SIMPLE AND COMPLEX SHAPES

SPS techniques have been used to produce near-net-shape sintered samples. Kuznetsova et al., report a square cross-section sintered aluminum-SiC composite sample [83], Maniere et al., have produced a thick variable thickness cylindrical sample with a sacrificial die component setup [58]. Maniere et al., also report the variations in grain sizes due to the variation in section thickness, it is reported that the sample location with a thinner section has porosity up to 20% compared to the fully dense regions [80]. It is reported that particle displacement is least in the thin section away from the moving punch. The density in this region is lowest. The prediction of relative density in complex shapes is discussed as a "shape factor" to account for temperature, relative density, and grain size spatial distribution. The temperature gradients present due to the non-circular cross-sections in complex shapes influence the local density of the sample [82]. The uniaxial pressure used in the SPS process is also not distributed over the surface of the sample, and grain growth in long residence time experiments contributes to grain growth variation.

Olevsky et al. have compared a prismatic sample to a cylindrical sample and found that the prismatic sample has approximately 10% less density, holding the SPS process parameters constant [82]. This microstructural evolution results in a corresponding evolution of the mechanical properties in accordance with the density gradients. Higher internal temperature gradients are calculated during SPS for high and very low aspect ratio samples [76]. For an alumina sample of 40 mm diameter and 10 mm thickness, a radial temperature gradient of about 20°C is predicted. Additional graphite felt coverage is suggested to reduce the internal temperature gradients [76]. Felt placement and coverage are studied to conclude that the properly placed and optimally positioned graphite felt heat shield helps in radial and axial temperature homogenization [76]. The mechanisms for improving the properties of sintered specimens require further research to accommodate the complex shapes and larger shaped specimens. Based on the heat flow lines (isotherms), the FEM-based approach must be used to optimize the mechanical designs as the trial and error technique can be cumbersome.

THERMOPHYSICAL PROPERTIES OF ALUMINUM AND ALUMINUM OXIDE COMPOSITES. HARDNESS AND MICROHARDNESS

Figure 4 presents the comparison of literature results for aluminum and aluminum alloy samples with varying reinforcing materials and their percentages. As can be seen, aluminum alloy samples have higher hardness compared to aluminum due to the alloying elements. In general, Al nanocomposite samples show higher hardness compared to Al microparticle samples due to the increased hardness of the nanoparticles and the high surface effects of the associated strengthening mechanism. Both positive increases and decreases in strength are evident from the literature. Some reasons mentioned include the presence of Al_4C_3 in the case of carbon-based reinforcements, such as CNT, graphene platelets, and graphene oxide. To overcome such a reactive compound, research is focused on coated CNTs. It is reported for CNT reinforcement that higher hardness can be achieved by reducing the surface reactions through copper coating [13]. Other reinforcements such as silicon carbide and boron nitride are reported to exhibit increased hardness [40, 44]. Alumina reinforcement is reported to show a non-linear increase in hardness with an increasing percentage of reinforcement [42].

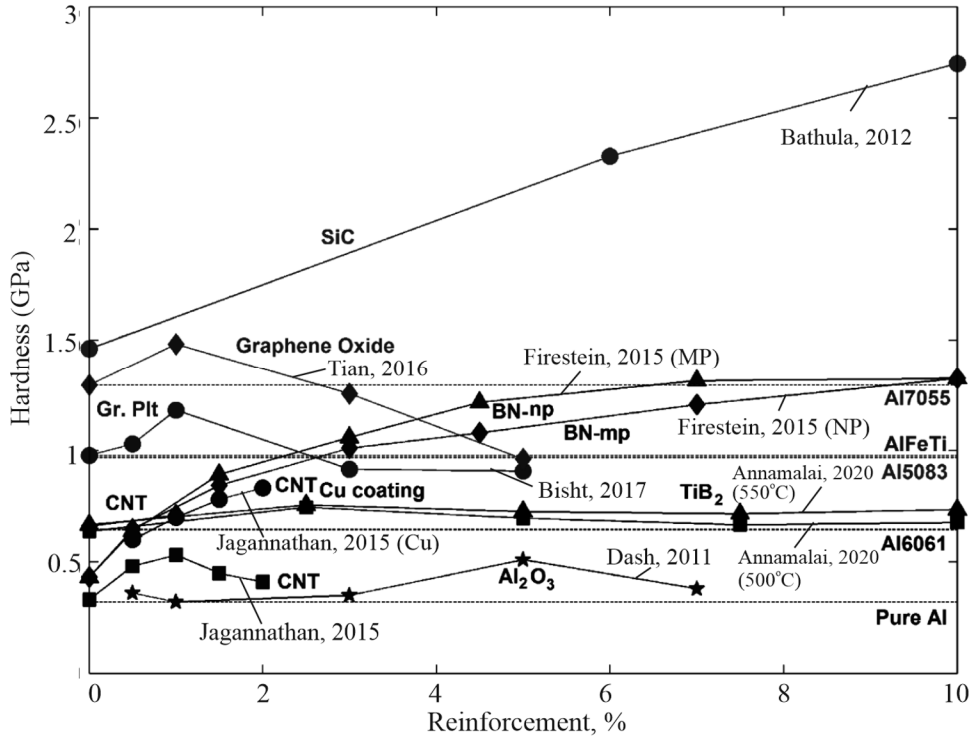

Fig. 4. Comparison of hardness vs. reinforcement content for aluminum samples

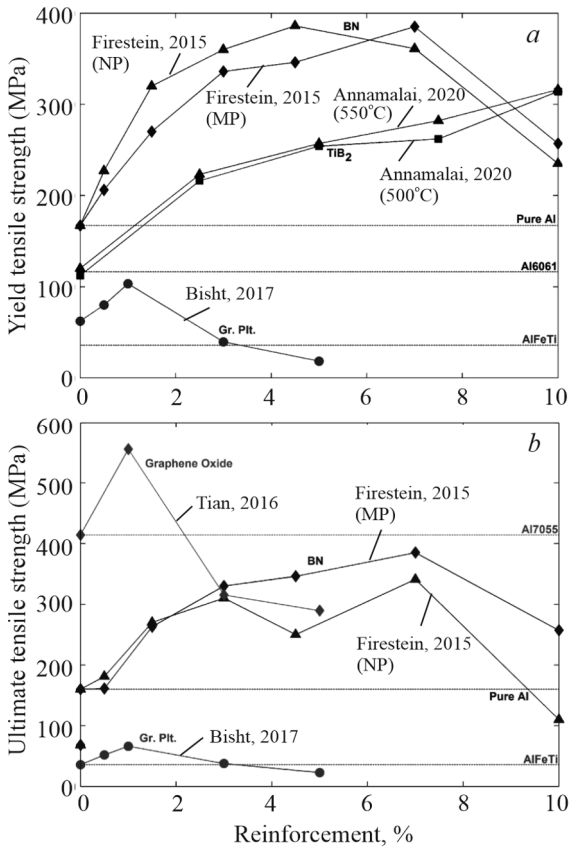

Fig. 5. Comparison of yield strength (*a*) and ultimate strength (*b*) vs. reinforcement content for SPS aluminum composite samples

Figures 5*a* and *b* compare the tensile strength and yield strength of SPS aluminum composites versus reinforcement. The trend exhibited by the SPS composites is similar to the hardness values of these samples. The yield strength increases at lower reinforcement percentages, typically less than 5%, and decreases at higher percentages. This general trend varies with different reinforcements, graphene oxide and graphene platelets with aluminum or aluminum alloys show higher yield strength at 1–2%. The crystalline carbonaceous reinforcements such as CNT, graphene oxide or graphene platelets show a strengthening mechanism similar to Orowan due to looping/stretching of graphene sheets and CNT shows telescopic stretching [27]. Carbonaceous reinforcements have a reactive bond with aluminum to form Al_4C_3, which is brittle and can be a strength reducer [27]. However, the trend for boron nitride is similar, although the peak yield and tensile strength occurs at about 5% reinforcement. Boron nitride forms a reactive bond with aluminum to form AlB_2 with a critical shear strength of 450 MPa. This may account for the increased yield and tensile strength of these composites [44]. In comparison, TiB_2 shows an increasing tensile yield strength up to 10% reinforcement. It has been reported that the density of the sinter material has a correlation with the hardness values [84]. Annamalai et al. also report the agglomeration of reinforcement particles, similar to other researchers. Particle agglomeration increases as the reinforcement percentage increases. The harder reinforcement particles counteract the dislocation density in the matrix material. This results in a reduction in elongation of the samples.

DISCUSSION OF THE RESULTS

Aluminum-based metal matrix composites can be produced by a variety of methods, but the SPS process has unique advantages for producing MMCs with unstable compositions. The SPS powder sintering process can produce higher quality composites than the metallurgical route because it does not suffer from density-dependent gradient formation and agglomeration. Uniform grain refinement, not possible with other techniques, is also achieved with the SPS process. SPS produces components with higher strength, hardness, and wear resistance compared to other metallurgical processes. Reinforcing materials with contrasting properties can be incorporated. SPS technique, due to its simultaneous application of high temperature, pressure, and electrical voltage, can break the surface oxide layer in aluminum particles and render bare surface-to-surface contact to achieve superior electrical and thermal properties. However, the improvement or degradation of the mechanical properties of the parts produced by SPS is determined by the presence of the surface oxide layer and the reinforcing nanomaterial. All the material properties of the aluminum and the reinforcing particles along with the process parameters used to determine the required properties of the component should be considered in the proposed applications for SPS.

Several SPS parameters, such as temperature, pressure, electrical pulse characteristics, and the SPS environment provided, as well as the method of mixing the reinforcement into the matrix, affect the mechanical, thermal, and electrical properties of samples prepared by SPS technique. In general, high energy ball milling is a common method to pulverize the particles to nanoscale sizes. Reinforcement is introduced by using solvents such as ethanol, isopropyl alcohol and DMF. These solvents reduce the agglomeration of the micro/nanoparticle reinforcement. Temperature has a greater effect on densification than pressure. The process pressure is dependent on the mold material. Composites close to bulk density can be produced using relevant SPS parameters. However, at high concentrations of carbon-based reinforcement, the reactive phase material produced by the SPS process tends to reduce the strength of the composite.

The SPS process is modeled to understand the importance of process parameters and to estimate the resulting mechanical properties of the produced samples using FEA and COMSOL Multiphysics software along with empirical correlations. Simulations are also used to understand material flow in graphite dies and grain size changes during the SPS process. Due to their superior properties, aluminum and alumina nanocomposites have found applications in a wide range of fields, including aerospace, hybrid vehicles, marine, and chemical equipment. However, the SPS process cannot accommodate the increasing component size and geometric complexity. Therefore, the development of a technology to implement SPS in complex geometries presents many opportunities for future researchers.

CONCLUSIONS WITH SCOPE OF RESEARCH IN SPS TECHNIQUE

A review of metal matrix composites based on aluminum and aluminum oxide based on the SPS technique is reported. Reinforcements including SiC, BN, CNT, GnP, Al_2O_3, ZrO_2, Y_2O_3, TiB_2 have been reviewed. Factors affecting the SPS process are also summarized. These include SPS environment, temperature and temperature ramp, pressure, electrical pulse pattern, and ageing of SPS samples. SPS tool design for aluminum samples is also reviewed. Mathematical modeling, with emphasis on densification behavior, for the aluminum and alumina SPS process is reviewed. The process of fabricating simple Aluminum MMC units using the SPS technique was investigated. The properties of SPS specimens including hardness, ultimate strength and tensile yield strength are compared to literature.

Concluding statements are as follows:

- The vacuum environment can inhibit additional oxidation of aluminum particles at elevated temperatures. The oxide layer already present on the surface increases the hardness of SPS samples.
- The sintering temperature has an effect on the final density of the SPS process. Selection depends on the melting point of the matrix. In particular, at temperatures above 450°C for aluminum samples and 1,250°C for alumina samples, densities close to 99% or higher can be achieved.
- The heating rate produces effects such as instantaneous densification, and heating rate should be chosen based on particle size, lower particle size requires slower temperature ramp.
- The applied pressure helps in breaching of surface oxide layer, and is limited by the die material. Graphite die is taken to 50 MPa or less, electrically conductive WC/Co die can be pressurized to 300 MPa.
- The applied pressure along with temperature leads to interfacial compounds such as, Al_4C_3 with carbonaceous reinforcements, AlN with nitride reinforcements, and AlB_2.
- The phenomenon of electrical sparking has been discussed in the literature. Particle gaps of less than 2 μm have a sufficiently low voltage difference to produce arcs and material necking due to the Townsend mechanism.
- Harder MMC sintered parts with complex shapes can be produced at mass production speeds using the SPS technique. However, the complex phenomenon of manufacturing MMCs using the SPS technique will require further research.

SCOPE OF RESEARCH IN SPS OF ALUMINA-REINFORCED ALUMINUM ALLOY (MMCS). SCALE UP AND INDUSTRIAL PRODUCTION

Traditionally, SPS requires specialized equipment and is not suitable for scaling up and mass-producing components. The pressure-less SPS (PLSPS) technique is used in conjunction with 3D printing to overcome the technical bottlenecks in producing complex shapes. However, mass production of dissimilar metal parts is not possible with this technique either. A rethinking of the basic SPS process is needed to make it more conducive to scale-up and industrial production.

Microstructure Control. Reinforcement particles tend to agglomerate during SPS processing of aluminum and alumina matrix. This leads to anomalies in the mechanical strength of the composites. Further research is needed to study and achieve proper particle dispersion, especially at higher reinforcement inclusion levels. The key to improving the strength of composites will be this microstructural control of binary and ternary combinations.

Sintering Mechanism and Deep Understanding of the Reinforcement Percentage. From the review, for the SPS process of alumina and pure aluminum matrix, the effect of process parameters is well understood. However, the percentage loading of carbon-based reinforcement has both positive and negative effects on hardness, yield and ultimate strength. This aspect of initial increase in mechanical properties at lower loading and subsequent decrease at higher loading can be investigated in future research.

Interfacial Bonding of Dissimilar Materials. The reaction layer between the reinforcement and matrix material plays a vital role in mechanical strength improvement of the composites. Reinforcements including high entropy alloys. and glassy materials are reported to improve the properties of composites. However, in order to

achieve the mechanical strength required for specific applications, further studies are required to assist in the careful refinement and tuning of interfacial bonding compositions.

Internal holes Structures and Features. The difficulty in producing internal holes and features using traditional SPS technique is well known. 3D printed graphite dies are reported in literature to accomplish the internal-hole features. Further investigation and understanding into the graphite die inclusions, dimensional stability needs to be studied.

Ageing of SPS Samples. The precipitation of alloying elements as a result of ageing has been reported in the literature. The annealing temperature is also reported to affect the micro-hardness of SPS samples. At higher annealing temperatures, the precipitation of alloying elements is reduced and the micro-hardness of the samples is initially reduced by ageing, but fully recovered over 500 days.

FEM Based Analysis. The absence of phase shift during the SPS process indicates that electrical pulse heating produces purely resistive heating. *In situ* changes in the properties of the graphite die are difficult to study experimentally, but the FEA approach confirms the weakening of the graphite die during the SPS process. The FEA tool can provide details of the densification behaviour during the SPS process. The main contributors are reported to be the internal stresses in the particles caused by the differential expansion of the particles and the die material. Updating the theories for hardness test simulation is warranted as models such as Hencky–Huber–Mises and Drucker–Prager models do not accurately predict the behaviour even in the elastic region.

Properties of MMNCs and Geometry of Components. The nanoparticle geometry is partly responsible for the increase in ultimate strength and micro-hardness of MMNCs. It is evident that the reinforcement of CNTs and graphene oxide at a concentration of 1% leads to the increase in strength due to the Orowan strengthening mechanism, but at higher concentrations it has the opposite effect and reduces the strength. The hardness behaviour of SPS MMNCs is further complicated by embrittlement due to the formation of reactive components such as Al_4C_3. Such complexities are not observed in the non-carbonaceous reinforcing materials.

Challenges in the SPS Process. The wear behaviour of the graphite die in relation to the applied pressure is not fully understood. Other electrically conductive ceramic die materials need to be developed to increase the applied pressure at lower temperatures and suitable electrical discharges. Lower power consumption and reduced set-up complexity can be achieved by developing pressureless SPS techniques for aluminium and alumina. The density variations in samples with complex shapes need to be better understood.

Graphene based aluminium composites have shown lower strength than the matrix material, the reasons for this phenomenon need to be understood. Harder MMC sintered components with complex shapes can be produced at mass production speeds using the SPS technique. However, further research will clarify the complex phenomenon of manufacturing MMCs using the SPS technique.

ARTICLE-LEVEL DECLARATIONS

Acknowledgements. The authors are thankful to M.S. Ramaiah University of Applied Sciences, Bangalore, Karnataka, India, for the encouragement and support in carrying out the research work.

Conflict of Interest. The authors of the study claim to be unaware of any financial or personal ties that might have influenced their study.

Funding. During the preparation of this work, the authors state that they did not receive any funding, grants, or other support of any kind.

Data Availability. The authors confirm that the data in support of the results of this study are available in the manuscript.

REFERENCES

1. P. Figiel, M. Rozmus, and B. Smuk, “Properties of alumina ceramics obtained by conventional and nonconventional methods for sintering ceramics,” *J. Achievements Mater. Manufact. Eng*., **48**, No. 1, 29–34 (2011).

2. P. Guyot, G. Antou, N. Pradeilles, A. Weibel, M. Vandenhende, G. Chevallier, A. Peigney, C. Estournès, and A. Maître, "Hot pressing and spark plasma sintering of alumina: Discussion about an analytical modelling used for sintering mechanism determination," *Scr. Mater.*, **84–85**, 35–38 (2014), doi:10.1016/j.scriptamat.2014.04.013.
3. Y. Aman, V. Garnier, and E. Djurado, "Spark plasma sintering kinetics of pure α-alumina," *J. Am. Ceram. Soc*. **94**, No. 9, 2825–2833 (2011), doi:10.1111/j.1551-2916.2011.04424.x.
4. R.G. Bhandare and P.M. Sonawane, "Preparation of aluminium matrix composite by using stir casting method," *Int. J. Eng. Adv. Technol*., **3**, No. 2, 6–65 (2013).
5. H. Abdizadeh, R. Ebrahimifard, and M.A. Baghchesara, Investigation of microstructure and mechanical properties of nano MgO reinforced Al composites manufactured by stir casting and powder metallurgy methods: A comparative study," *Compos. Part. B Eng*., **56**, 217–221 (2014), doi:10.1016/j.compositesb.2013.08.023.
6. A. Azarniya, A. Azarniya, S. Sovizi, H.R.M. Hosseini, T. Varol, A. Kawasaki, and S. Ramakrishna, "Physicomechanical properties of spark plasma sintered carbon nanotube-reinforced metal matrix nanocomposites," *Prog. Mater. Sci*., **90**, 276–324 (2017), doi:10.1016/j.pmatsci.2017.07.007.
7. N. Saheb, "Spark plasma and microwave sintering of Al6061 and Al2124 alloys," *Int. J. Miner. Metall. Mater*., **20**, No. 2, 152–159 (2013), doi:10.1007/s12613-013-0707-6.
8. P. Cavaliere, *Spark Plasma Sintering of Materials,* Springer Nature Switzerland, Springer Cham. (2019), doi:10.1007/978-3-030-05327-7.
9. S. Sovizi and M.E. Seraji, "The densification behavior of metals and alloys during spark plasma sintering: A mini-review," *Sci. Sinter*., **51**, No. 2, 1–18 (2019), doi:10.2298/sos1902135s.
10. K. Mizuuchi, K. Inoue, Y. Agari, M. Tanaka, T. Takeuchi, J. Tani, M. Kawahara, Y. Makino, and M. Ito, "Effects of bimodal and monomodal SiC particle on the thermal properties of SiC-particle-dispersed Al-matrix composite fabricated by SPS," *J. Metall. Eng*., **5 (**2016), doi:10.14355/me.2016.05.001.
11. A. Haque, S. Shekhar, S.V.S. Narayana Murty, J. Ramkumar, K. Kar, and K. Mondal, "Fabrication of controlled expansion Al–Si composites by pressureless and spark plasma sintering," *Adv. Powder Technol*., **29**, No. 12, 3427–3439 (2018), doi:10.1016/j.apt.2018.09.024.
12. D. Giuntini, E.A. Olevsky , C. Garcia-Cardona , A.l. Maximenko, M.S. Yurlova, C.D. Haines, D.G. Martin, and D. Kapoor, "Localized overheating phenomena and optimization of spark-plasma sintering tooling design," *Materials (Basel)*, **6**, No. 7, 2612–2632 (2013), doi:10.3390/ma6072612.
13. M. Jagannatham, S. Sankaran, and P. Haridoss, "Microstructure and mechanical behavior of copper coated multiwall carbon nanotubes reinforced aluminum composites," *Mater. Sci. Eng. A*, **638**, 197–207 (2015), doi:10.1016/j.msea.2015.04.070.
14. A.M.K. Esawi, K. Morsi, A. Sayed, M. Taher, and S. Lanka, "Effect of carbon nanotube (CNT) content on the mechanical properties of CNT-reinforced aluminium composites," *Compos. Sci. Technol*., **70**, No. 16, 2237–2241 (2010), doi:10.1016/j.compscitech.2010.05.004.
15. S.R. Bakshi, D. Lahiri, and A. Agarwal, "Carbon nanotube reinforced metal matrix composites—A review," *Int. Mater. Rev*., **55**, No. 1, 41–64 (2010), doi:10.1179/095066009X12572530170543.
16. A. Esmaeilzaei, S.A. Sajjadi, S. Mollazadeh Beidokhti, and H. Beygi, "Rapid consolidation of Al_2O_3–TiO_2–Co nanocermets via spark plasma sintering of Co-coated ceramic particles," *J. Alloys Compd*., **771**, 79–88 (2019), doi:10.1016/j.jallcom.2018.08.249.
17. S.R. Bakshi, V. Singh, S. Seal, and A. Agarwal, "Aluminum composite reinforced with multiwalled carbon nanotubes from plasma spraying of spray dried powders," *Surf. Coat. Technol*., **203**, No. 10–11, 1544–1554 (2009), doi:10.1016/j.surfcoat.2008.12.004.
18. S.R. Bakshi, V. Singh, K. Balani, D.G. McCartney, S. Seal, and A. Agarwal, "Carbon nanotube reinforced aluminum composite coating via cold spraying," *Surf. Coat. Technol*., **202**, No. 21, 5162–5169 (2008), doi:10.1016/j.surfcoat.2008.05.042.

19. J. Liao and M.J. Tan, “Mixing of carbon nanotubes (CNTs) and aluminum powder for powder metallurgy use,” *Powder Technol*., **208**, No. 1, 42–48 (2011), doi:10.1016/j.powtec.2010.12.001.
20. T. Noguchi, A. Magario, S. Fukazawa, S. Shimizu, J. Beppu, and M. Seki, “Carbon nanotube/aluminium composites with uniform dispersion,” *Mater. Trans*., **45**, No. 2, 602–604 (2004), doi:10.2320/matertrans.45.602.
21. T. Laha, A. Agarwal, T. McKechnie, and S. Seal, “Synthesis and characterization of plasma spray formed carbon nanotube reinforced aluminum composite,” *Mater. Sci. Eng. A*, **381**, No. 1–2, 249–258 (2004), doi:10.1016/j.msea.2004.04.014.
22. I.K. Aliyu, N. Saheb, S.F. Hassan, and N. Al-Aqeeli, “Microstructure and properties of spark plasma sintered aluminum containing 1 wt.% SiC nanoparticles,” *Metals (Basel)*, **5**, No. 1, 70–83 (2015), doi:10.3390/met5010070.
23. C. Zhang, Z. Cai, R. Wang, C. Peng, K. Qiu, and N. Wang, “Microstructure and thermal properties of Al/W-coated diamond composites prepared by powder metallurgy,” *Mater. Des*., **95**, 39–47 (2016), doi:10.1016/j.matdes.2016.01.085.
24. Z. Yuan, W. Tian, F. Li, Q. Fu, Y. Hu, and X. Wang, “Microstructure and properties of high-entropy alloy reinforced aluminum matrix composites by spark plasma sintering,” *J. Alloys Compd*., **806** (August), 901–908 (2019), doi:10.1016/j.jallcom.2019.07.185.
25. K.E. Thomson, D. Jiang, W. Yao, R.O. Ritchie, and A.K. Mukherjee, “Characterization and mechanical testing of alumina-based nanocomposites reinforced with niobium and/or carbon nanotubes fabricated by spark plasma sintering,” *Acta Mater*., **60**, No. 2, 622–632 (2012), doi:10.1016/j.actamat.2011.10.002.
26. G.D. Zhan, J. Kuntz, J. Wan, J. Garay, and A.K. Mukherjee, “Alumina-based nanocomposites consolidated by spark plasma sintering,” *Scr. Mater*., **47**, No. 11, 737–741 (2002), doi: 10.1016/S1359-6462(02)00191-4.
27. B. Boesl, D. Lahiri, S. Behdad, and A. Agarwal, “Direct observation of carbon nanotube induced strengthening in aluminum composite via in situ tensile tests,” *Carbon,* **69**, 79–85 (2014), doi: 10.1016/j.carbon.2013.11.061.
28. Z.Y. Hu, Z.H. Zhang, X.W. Cheng, F.C. Wang, Y.F. Zhang, and S.L. Li, “A review of multi-physical fields induced phenomena and effects in spark plasma sintering: Fundamentals and applications,” *Mater. Des*., **191 (**2020), doi:10.1016/j.matdes.2020.108662.
29. G.Z. Quan, K.W. Liu, J. Zhou, and B. Chen, “Dynamic softening behaviors of 7075 aluminum alloy,” *Trans Nonferrous Met. Soc. China (English Ed*.), **19** (SUPPL. 3), s537–s541 (2009), doi: 10.1016/S1003-6326(10)60104-5.
30. A.S. Iyengar, D. Liang, X.P.A. Gao, and A.R. Abramson, “Densification effects on the electrical behavior of uniaxially compacted bismuth nanowires,” *Acta Mater*., **60**, No. 5, 2369–2378 (2012), doi:10.1016/j.actamat.2011.12.020.
31. S.R. Hostler, A.S. Iyengar, N.K. Mahanta, and A.R. Abramson, “Thermal conductivity of cold compacted bismuth nanowires,” *Int. J. Heat. Mass. Transf*., **117**, 951–957 (2018), doi:10.1016/j.ijheatmasstransfer.2017.10.066.
32. A.S. Chua, M. Brochu, and D.P. Bishop, “Spark plasma sintering of prealloyed aluminium powders,” *Powder Metall*., **58**, No. 1, 51–60 (2015), doi:10.1179/1743290114Y.0000000105.
33. G.A. Sweet, *Advanced Sintering Techniques for Aluminium: Spark Plasma Sintering*, Dalhousie University Halifax (Nova Scotia), 2014, doi:hdl.handle.net/10222/54025.
34. M. Razavi, A.R. Farajipour, M. Zakeri, M.R. Rahimipour, and A.R. Firouzbakht, “Production of Al_2O_3–SiC nano-composites by spark plasma sintering,” *Boletín de la Sociedad Española de Cerámica y Vidrio*, **56**, No. 4, 186–194 (2017), doi:10.1016/j.bsecv.2017.01.002.
35. M.H. Bocanegra-Bernal, C. Dominguez-Rios, J. Echeberria, A. Reyes-Rojas, A. Garcia-Reyes, and A. Aguilar-Elguezabal, “Spark plasma sintering of multi-, single/double- and single-walled carbon nanotube-reinforced alumina composites: Is it justifiable the effort to reinforce them?”, *Ceram. Int*., **42**, No. 1, 2054–2062 (2016), doi:10.1016/j.ceramint.2015.09.060.

36. J. Echeberria, N. Rodríguez, J. Vleugels, K. Vanmeensel, A. Reyes-Rojas, A. Carcia-Reyes , C. Dominguez-Rios, A. Aguilar-Elguezabal, and M.H. Bocanegra-Bernal, "Hard and tough carbon nanotube-reinforced zirconia-toughened alumina composites prepared by spark plasma sintering," *Carbon*, **50**, No. 2, 706–717 (2012), doi:10.1016/j.carbon.2011.09.031.
37. B.N. Kim, K. Hiraga, S. Grasso, K. Morita, H. Yoshida, H. Zhang, and Y. Sakka, "High-pressure spark plasma sintering of MgO-doped transparent alumina," *J. Ceram. Soc. Japan*, **120**, No. 1399, 116–118 (2012), doi:10.2109/jcersj2.120.116.
38. K.A. Khor, L.G. Yu, Y. Li, Z.L. Dong, and Z.A. Munir, "Spark plasma reaction sintering of ZrO_2-mullite composites from plasma spheroidized zircon/alumina powders," *Mater. Sci. Eng. A*, **339**, No. 1–2, 286–296 (2003), doi:10.1016/S0921-5093(02)00151-X.
39. Kaspar Kallip, Marc Leparoux, Khaled A. AlOgab, Xavier Maeder, Yadira Arroyo Rojas Dasilva, "Influence of microstructure and strengthening mechanism of AlMg5–Al_2O_3 nanocomposites prepared via spark plasma sintering," *Mater. Des*., **95**, 534–544 (2016), doi:10.1016/j.matdes.2016.01.138.
40. S. Bathula, R.C. Anandani, A. Dhar, and A.K. Srivastava, "Microstructural features and mechanical properties of Al5083/SiCp metal matrix nanocomposites produced by high energy ball milling and spark plasma sintering," *Mater. Sci. Eng. A*, **545**, 97–102 (2012), doi:10.1016/j.msea.2012.02.095.
41. A. Bisht, M. Srivastava, R.M. Kumar, I. Lahiri, and D. Lahiri, "Strengthening mechanism in graphene nanoplatelets reinforced aluminum composite fabricated through spark plasma sintering," *Mater. Sci. Eng. A*, **695**, March, 20–28 (2017), doi:10.1016/j.msea.2017.04.009.
42. K. Dash, D. Chaira, and B.C. Ray, *Synthesis and Characterization of Aluminium-Alumina Micro- and Nano-Composites by Spark Plasma Sintering*, Elsevier Ltd, Vol. 48 (2013). doi:10.1016/j.materresbull.2013.03.014.
43. A. Eldesouky, M. Johnsson, H. Svengren, M.M. Attallah, and H.G. Salem, "Effect of grain size reduction of AA2124 aluminum alloy powder compacted by spark plasma sintering," *J. Alloys Compd*., **609**, 215–221 (2014), doi:10.1016/j.jallcom.2014.04.136.
44. K.L. Firestein, A.E. Steinman, I.S. Golovin, J. Cifre, E. Obraztsova, A.T. Matveev, A. Kovalskii, O. Lebedev, D.V. Shtansky, and D. Colberg, "Fabrication, characterization, and mechanical properties of spark plasma sintered Al–BN nanoparticle composites," *Mater. Sci. Eng. A*, **642**, 104–112 (2015), doi:10.1016/j.msea.2015.06.059.
45. E. Ghasali, H. Nouranian, A. Rahbari, H. Majidian, M. Alizadeh, and T. Ebadzadeh, "Low temperature sintering of aluminum-zircon metal matrix composite prepared by spark plasma sintering," *Mater. Res*., **19**, No. 5, 1189–1192 (2016), doi:10.1590/1980-5373-MR-2016-0395.
46. Ehsan Ghasali, Kamyar Shirvanimoghaddamb, Masoud Alizadeha, and Touradj Ebadzadeh, "Ultra-low temperature fabrication of vanadium carbide reinforced aluminum nano composite through spark plasma sintering," *J. Alloys Compd*., **753**, 433–445 (2018).
47. S. Grasso, B.N. Kim, C. Hu, G. Maizza, and Y. Sakka, "Highly transparent pure alumina fabricated by high-pressure spark plasma sintering," *J. Am. Ceram. Soc*., **93**, No. 9, 2460–2462 (2010), doi:10.1111/j.1551-2916.2010.03811.x.
48. F. Inam, H. Yan, D.D. Jayaseelan, T. Peijs, and M.J. Reece, "Electrically conductive alumina-carbon nanocomposites prepared by Spark Plasma Sintering," *J. Eur. Ceram. Soc*., **30**, No. 2, 153–157 (2010), doi:10.1016/j.jeurceramsoc.2009.05.045.
49. A. Pavia, L. Durand, F. Ajustron, V. Bley, G. Chevallier, A. Peigney, and C. Estournès, "Electro-thermal measurements and finite element method simulations of a spark plasma sintering device," *J. Mater. Proc. Technol*., **213**, No. 8, 1327–1336 (2013), doi:10.1016/j.jmatprotec.2013.02.003.
50. G. Molénat, L. Durand, J. Galy, and A. Couret, "Temperature control in spark plasma sintering: An FEM approach," *J. Metall*., **2010**, No. 1, 1–9 (2010), doi:10.1155/2010/145431.
51. N. Seetala, O. Reedy, L. Matson, H.D. Lee, and T. Key, "Effect of argon gas purging of spark plasma sintered ZrB_2 + SiC nano-powder composites," *Miner. Met. Mater. Ser*., Part F7, 171–178 (2017), doi:10.1007/978-3-319-51382-9_19.

52. D. Paraskevas, K. Vanmeensel, J. Vleugels, W. Dewulf, Y. Deng, and J.R. Duflou, "Spark plasma sintering as a solid-state recycling technique: The case of aluminum alloy scrap consolidation," *Materials (Basel)*, **7**, No. 8, 5664–5687 (2014), doi:10.3390/ma7085664.
53. H. Kwon, D.H. Park, Y. Park, J.F. Silvain, A. Kawasaki, and Y. Park, "Spark plasma sintering behavior of pure aluminum depending on various sintering temperatures," *Met. Mater. Int*., **16**, No. 1, 71–75 (2010), doi:10.1007/s12540-010-0071-2.
54. A. Khalil, A.S. Hakeem, and N. Saheb, "Optimization of process parameters in spark plasma sintering Al6061 and Al2124 aluminum alloys," *Adv. Mater. Res*., **328–330**, September, 1517–1522 (2011), doi:10.4028/www.scientific.net/AMR.328-330.1517.
55. G.A. Sweet, M. Brochu, R.L. Hexemer, I.W. Donaldson, and D.P. Bishop, "Consolidation of aluminum-based metal matrix composites via spark plasma sintering," *Mater. Sci. Eng. A*, **648**, 123–133 (2015), doi:10.1016/j.msea.2015.09.027.
56. B. Ratzker, M. Sokol, S. Kalabukhov, and N. Frage, "Using a spark plasma sintering apparatus as a tool in a compressive creep study of fine-grained alumina," *Ceram. Int*., **43**, No. 12, 9369–9376 (2017), doi:10.1016/j.ceramint.2017.04.106.
57. J.G. Santanach, A. Weibel, C. Estourns, Q. Yang, C. Laurent, and A. Peigney, "Spark plasma sintering of alumina: Study of parameters, formal sintering analysis and hypotheses on the mechanism(s) involved in densification and grain growth," *Acta Mater*., **59**, No. 4, 1400–1408 (2011), doi:10.1016/j.actamat.2010.11.002.
58. C. Manière, L. Durand, G. Chevallier, and C. Estournès, "A spark plasma sintering densification modeling approach: From polymer, metals to ceramics," *J. Mater. Sci*., **53**, No. 10, 7869–7876 (2018), doi:10.1007/s10853-018-2096-8.
59. Omkar Bamane, Sanket Patil, Lucky Agarwal, and P. Kuppan, "Fabrication and characterization of AA7075 metal matrix composite reinforced with MWCNT," *Materials Today: Proceedings*, **5**, No. 2, 8001–8007 (2018), doi: 10.1016/j.matpr.2017.11.484.
60. J.E. Garay, "Current-activated, pressure-assisted densification of materials," *Annu Rev Mater Res*., **40**, 445–468 (2010), doi: 10.1146/annurev-matsci-070909-104433.
61. O. Guillon, J. Gonzalez-Julian, B. Dargatz, T. Kessel, G. Schierning, J. Rathel, and M. Herrmann, "Field-assisted sintering technology/spark plasma sintering: Mechanisms, materials, and technology developments," *Adv. Eng. Mater*., **16**, Issue 7, 830–849 (2014), doi:10.1002/adem.201300409.
62. Y. Aman, V. Garnier, and E. Djurado, "Pressure-less spark plasma sintering effect on non-conventional necking process during the initial stage of sintering of copper and alumina," *J. Mater. Sci*. **47**, No. 15, 5766–5773 (2012), doi:10.1007/s10853-012-6469-0.
63. G. Ji, Z.Q. Tan, Z.Q. Li, R. Shabadi, A. Addad, J.-F. Silvain, and D. Zhang, "Understanding and tailoring interfacial bonding states of a diamond/AL composite for thermal management applications," in: *21st Int. Conference on Composite Materials* (Xi'an, 20–25th August, 2017).
64. Z.Y. Hu, Z.H. Zhang, H. Wang, S.-L. Li, S.-P. Yin, Q. Song, and X. Cheng, "A rapid route for synthesizing Ti–(Al_xTi_y/UFG Al) core-multishell structured particles reinforced Al matrix composite with promising mechanical properties," *Mater. Sci. Eng. A*, **721**, 61–64 (2018), doi:10.1016/j.msea.2018.02.065.
65. E.A. Olevsky and L. Froyen, "Impact of thermal diffusion on densification during SPS," *J. Am. Ceram. Soc*., **92**, SUPPL. 1, 122–132 (2009), doi:10.1111/j.1551-2916.2008.02705.x.
66. R. Tirumala and D.B. Go, "An analytical formulation for the modified Paschen's curve," *Appl. Phys. Lett*., **97**, No. 15, 13–16 (2010), doi:10.1063/1.3497231.
67. R.S. Dhariwal, J.M. Torres, and M.P.Y. Desmulliez, "Electrical field breakdown at micrometer separations in air and nitrogen at atmospheric pressure," *IEE Proc. Sci. Meas. Technol*., **147**, No. 5, 261–265 (2000).
68. M. Radmilović-Radjenović and B. Radjenović, "Theoretical study of the electron field emission phenomena in the generation of a micrometer scale discharge," *Plasma Sources Sci. Technol*., **17**, No. 2 (2008), doi:10.1088/0963-0252/17/2/024005.

69. H.J. Ryu, S.I. Cha, and S.H. Hong, "Generalized shear-lag model for load transfer in SiC/Al metal-matrix composites," *J Mater. Res*., **18**, No. 12, 2851–2858 (2003), doi:10.1557/JMR.2003.0398.
70. Z. Zhang and D.L. Chen, "Consideration of Orowan strengthening effect in particulate-reinforced metal matrix nanocomposites: A model for predicting their yield strength," *Scr. Mater*., **54**, No. 7, 1321–1326 (2006), doi:10.1016/j.scriptamat.2005.12.017.
71. O. Molnárová, P. Málek, F. Lukáč, and T. Chráska, "Spark plasma sintering of a gas atomized Al7075 alloy: Microstructure and properties," *Materials (Basel)*, **9**, No. 12, 1–15 (2016), doi:10.3390/ma9121004.
72. A. Fadavi Boostani, S. Yazdani, R. Taherzadeh Mousavian, S. Tahamtan, R. Azari Khosroshahi, D. Wei, D. Brahazon, J.Z. Xu, X.M. Zhang, and Z.Y. Jiang, "Strengthening mechanisms of graphene sheets in aluminium matrix nanocomposites," *Mater. Des*., **88**, 983–989 (2015), doi:10.1016/j.matdes.2015.09.063.
73. G.K. Meenashisundaram, M.H. Nai, and M. Gupta, "Effects of primary processing techniques and significance of hall-petch strengthening on the mechanical response of magnesium matrix composites containing TiO_2 nanoparticulates," *Nanomaterials*, **5**, No. 3, 1256–1283 (2015), doi:10.3390/nano5031256.
74. F.A. Mirza and D.L. Chen, "A unified model for the prediction of yield strength in particulate-reinforced metal matrix nanocomposites," *Materials (Basel)*, **8**, No. 8, 5138–5153 (2015), doi:10.3390/ma8085138.
75. A. Bisht, M. Srivastava, R.M. Kumar, I. Lahiri, and D. Lahiri, "Strengthening mechanism in graphene nanoplatelets reinforced aluminum composite fabricated through spark plasma sintering," *Mater. Sci. Eng. A*, **695** (April), 20–28 (2017), doi:10.1016/j.msea.2017.04.009.
76. Y. Achenani, M. Saâdaoui, A. Cheddadi, G. Bonnefont, and G. Fantozzi, "Finite element modeling of spark plasma sintering: Application to the reduction of temperature inhomogeneities, case of alumina," *Mater. Des*., **116**, 504–514 (2017), doi:10.1016/j.matdes.2016.12.054.
77. S. Muñoz and U. Anselmi-Tamburini, "Temperature and stress fields evolution during spark plasma sintering processes," *J. Mater. Sci*., **45**, No. 23, 6528–6539 (2010), doi:10.1007/s10853-010-4742-7.
78. G. Bolzon, E.J. Chiarullo, P. Egizabal, and C. Estournes, "Constitutive modelling and mechanical characterization of aluminium-based metal matrix composites produced by spark plasma sintering," *Mech. Mater*., **42**, No. 5, 548–558 (2010), doi:10.1016/j.mechmat.2010.03.001.
79. C. Manière, L. Durand, A. Weibel, G. Chevallier, and C. Estournès, "A sacrificial material approach for spark plasma sintering of complex shapes," *Scr. Mater*., **124**, 126–128 (2016), doi:10.1016/j.scriptamat.2016.07.006.
80. C. Manière, L. Durand, A. Weibel, and C. Estournès, "Spark-plasma-sintering and finite element method: From the identification of the sintering parameters of a submicronic α-alumina powder to the development of complex shapes," *Acta Mater*., **102**, 169–175 (2016), doi:10.1016/j.actamat.2015.09.003.
81. Y. Xiong, D. Liu, Y. Li, B. Zheng, C. Heines, J. Paras, D. Martin, D. Kapoor, E. Levernia, and J.M. Schoenung, "Spark plasma sintering of cryomilled nanocrystalline Al alloy. Part I: Microstructure evolution," *Metall. Mater. Trans. A Phys. Metall. Mater. Sci*., **43**, No. 1, 327–339 (2012), doi:10.1007/s11661-011-0933-3.
82. E. Olevsky, E. Khaleghi, C. Garcia, and W. Bradbury, "Fundamentals of spark-plasma sintering: Applications to net-shaping of high strength temperature resistant components," *Mater. Sci. Forum*, **654–656**, 412–415 (2010), doi: 10.4028/www.scientific.net/MSF.654-656.412.
83. E. Kuznetsova, P. Peretyagin, A. Smirnov, W. Solis, and R. Torrecillas, "Near-net shapes Al_2O_3–SiCw ceramic nanocomposites produced by hybrid spark plasma sintering," in: *Proceedings of the Scientific-Practical Conference "Research and Development-2016*" (2018), pp. 397–404, doi: 10.1007/978-3-319-62870-7_42.
84. A. Raja Annamalai, Muthe Srikanth, A. Muthuchamy, Shashank Acharya, Anup Khisti, Dinesh K. Agrawal, and Chun-Ping Jen, "Spark plasma sintering and characterization of Al–TiB_2 composites," *Metals (Basel)*, **10**, No. 9, 1–12 (2020), https://doi.org/10.3390/met10091110.